*Revised Manuscript
Click here to view linked References

Plasma-induced Redox Reactions Synthesis of Nanosized α-, γ- and δ-MnO_2 Catalysts for Dye Degradation

Franck W. Boyom-Tatchemo [a,b], François Devred [b], G. Ndiffo-Yemeli [a], Samuel Laminsi [a] and Eric M. Gaigneaux [b*]

[a] Inorganic Chemistry Department, University of Yaoundé I, P.O. Box 812, Yaoundé, Cameroon

[b] Institute of Condensed Matter and Nanosciences (IMCN), Division Molecular Chemistry, Materials and Catalysis (MOST), UCLouvain, Place Louis Pasteur 1, box L4.01.09, B-1348 Louvain-la-Neuve, Belgium

Mesoporous α- and δ-MnO_2 with specific surface areas of 98 and 186 m^2/g, were obtained via plasmachemical-reduction of $KMnO_4$ solutions induced by flashing them with a gliding arc plasma operated at respectively high and low voltages. Correspondingly, γ- and δ-MnO_2 with 48 and 289 m^2/g, were obtained via plasmachemical-oxidation of $Mn(CH_3COO)_3$ solutions. At lower humid airflow, the plasma also led during the reduction of $KMnO_4$ to changes of structure and morphology, and to increased specific surface areas. These changes are hypothesized to be due to a variation of the amount of radicals generated by the plasma along its creation parameters. Performances of the prepared catalysts were evaluated in the oxidation of Tartrazin Yellow (TY) chosen as a model dye polluting wastewaters. TY bleaching was significantly different from one plasma-synthesized material to another. α-MnO_2, being the best of the plasma synthesized material appears to be recyclable and resistant to dissolution. This contribution confirms the importance of mastering the structure and texture of MnO_2 catalysts during their synthesis. Gliding arc plasma is revealed as an easy and efficient method to achieve so.

Keywords: Plasmachemical synthesis, Mesoporous manganese oxide, Gliding arc plasma, Tartrazin Yellow.

1. Introduction

Synthesis of nanomaterials with the control of their crystallinity, porosity, and morphology by varying simple parameters of their synthesis as temperature, voltage and pH, has now become a major challenge to maximize their performance in various industrial applications, including

optics, magnetism, and catalysis [1-3]. For decades, manganese oxides (MnO, Mn_3O_4, Mn_2O_3, and MnO_2) have attracted considerable interest from researchers, because of their interesting physicochemical properties, and potential applications [4]. Among them, nanostructured manganese dioxide (MnO_2) has received great attention because of its potential as heterogeneous catalyst and photocatalyst in advanced oxidation processes (AOPs) aiming at efficient elimination of pollutants [5, 6]. It is also appreciated because of its low cost, and environmental friendliness [7, 8]. MnO_2 exists in various polymorphs such as α-, β-, γ-, δ-, ε-, and λ-MnO_2, differing by the arrangement of their MnO_6 octahedra [9]. Many processes have been proposed to synthesize nanostructured MnO_2, such as solid-state reaction, sol-gel, co-precipitation, thermal decomposition, and hydrothermal method [1, 3, 10-14]. However, these methods often require complex procedures, high synthesis temperatures, long times, and are expensive [15, 16].

The use of gliding arc plasma (glidarc) has been shown as an alternative approach to prepare oxides [17]. When created with humid air as feed gas, the glidarc discharge indeed generates, at atmospheric pressure and quasi-ambient temperature, $HO^{\cdot}$ and $NO^{\cdot}$ radicals as main species [17, 18]. Details on the genesis of these radicals may be found in [18-20]. When directed to metallic aqueous solutions, thanks to the oxidizing ($HO^{\cdot}$) and reducing ($NO^{\cdot}$) characters of the radicals it contains, the discharge induces the precipitation of the corresponding metal (hydr)oxides. For example, Acayanka et al., and Tiya-Djowe et al. synthesized nanostructures of titanium dioxide and iron(III) oxy(hydroxide) via plasmachemical oxidations of respectively Ti(III) and Fe(II) solutions [19, 20]. Also, we showed the reducing capability of gliding arc plasma and its ability to precipitate manganese dioxide from a Mn(VII) solution [21].

Moving one step further, we now (i) demonstrate the possibility to glidarc-precipitate MnO_2 not only by reduction, but also by an oxidation route, and (ii) illustrate the impact that easily accessible gliding arc plasma parameters have on the final characteristics of the plasma-synthesized products. More precisely, here we explore how to exploit the combined oxidation-reduction properties of the glidarc discharge to easily synthesize various polymorphs of MnO_2 via the reduction of $KMnO_4$ solutions *vs* the oxidation of $Mn(CH_3COO)_3.2H_2O$ ones. We also explore the impact of the voltage and airflow at which the glidarc is operated on the texture and structure of the plasma-synthesized solids. The prepared materials were characterized by X-ray diffraction (XRD), Raman spectroscopy, Fourier transform infrared (FTIR), thermogravimetric analysis (TGA), X-ray photoelectron spectroscopy (XPS), nitrogen physisorption, and scanning electron microscopy (SEM). Catalytic performances of the different Mn oxides prepared were

then evaluated in the bleaching/degradation of Tartrazin Yellow (TY), the latter being chosen as a model organic pollutant of industrial dye containing-wastewaters.

2. Experimental section

2.1 Synthesis device: the gliding arc plasma reactor

The device generating the gliding arc plasma is represented on figure 1. To produce the discharge, air was used as feed gas and brought by a compressor at a flow that was varied in our experiments between 800 or 600 L/h; the air was humidified *via* its bubbling in a vessel containing distilled water at room temperature, before it was injected along the electrodes through a nozzle. The electric arc is formed at the smallest gap (3mm) between the electrodes which are biased (low voltage noted "LV" 480 or high voltage noted "HV" 600 V, 160 mA) thanks to an AC generator. The arc is pushed away by the humid air flow, and glides along the electrodes until it collapses. Arcs form one after the other, the collection of arcs forming a large plasma plume in contact with the liquid surface.

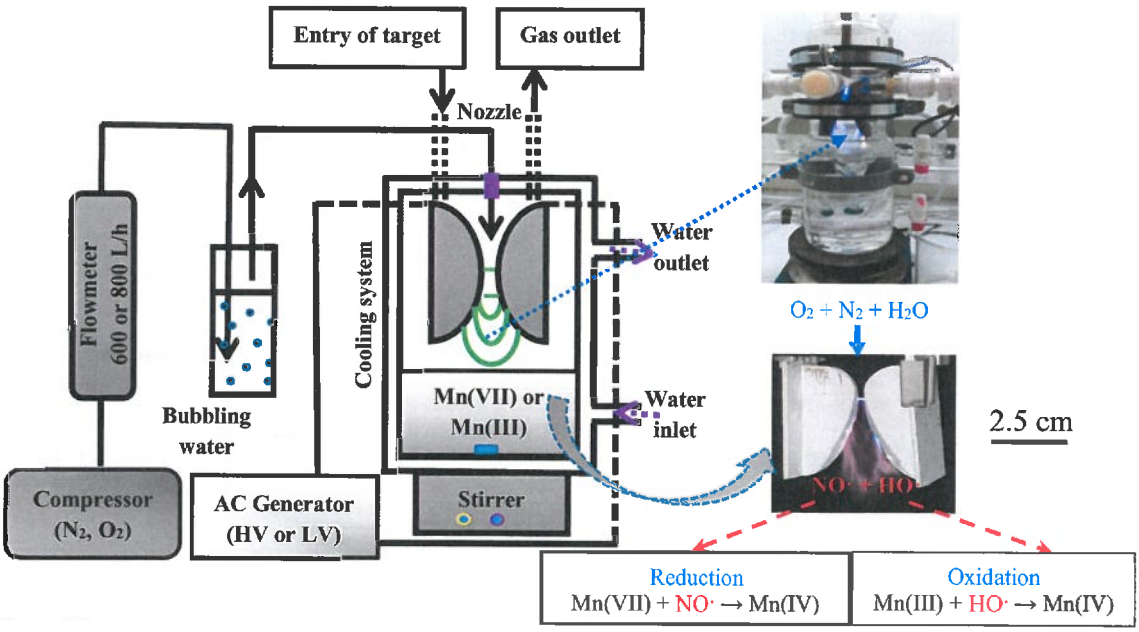


Fig. 1 Scheme of the gliding arc plasma setup.

2.2 Materials Synthesis

$KMnO_4$ (97%) and $Mn(CH_3COO)_3.2H_2O$ (97%) were purchased from SIGMA-ALDRICH. The precursors solutions have been prepared by dissolving 1.2g of $KMnO_4$ in 2L of de-ionized water, while 1g of $Mn(CH_3COO)_3.2H_2O$ was dissolved in 500 mL of a mixture of acetic acid (95%) and de-ionized water (ratio 1/21). The target solutions of $KMnO_4$ (450 mL, 700 mg/L),

and $Mn(CH_3COO)_3.2H_2O$ (450 mL, 2000 mg/L) were introduced and magnetically stirred into the reactor core and exposed at ambient temperature (25°C) and atmospheric pressure to the plasma discharge, created at 600V or 480V, with an airflow of 800L/h; exposure was maintained until complete precipitation. In parallel, target solutions of $KMnO_4$ (450 mL, 700 mg/L) were exposed to the gliding arc plasma discharge, created at HV, with an airflow of 600 L/h. Brown-black precipitates were obtained after all the exposures and recovered by filtration, washed with de-ionized water, and dried at 105°C in air. A nomenclature as Red/HV (standing for "Reduction at high voltage"), Oxi/HV ("Oxidation at high voltage"), Red/LV ("Reduction at low voltage") and Oxi/LV ("Oxidation at low voltage") is used hereafter to name the materials precipitated under these conditions.

2.3 Characterization techniques

X-ray diffraction patterns of the different materials were recorded between 5 and 80° at the rate of 0.6°/min with an increment of 0.02° and an integration time of 2s using a Kristalloflex Siemens D5000 diffractometer, operating at 40 kV and 40 mA, with the Cu K_α radiation (0.15418 nm). The powdered samples were deposited on "zero noise" polished Si sample holders slightly impregnated with handcream. The ICDD-JCPDS database was used to identify the crystalline phases. Raman spectroscopy was carried out using a Bruker RFS 100IS, equipped with a 532 nm excitation laser (10 mW), and working with 4 cm^{-1} as resolution. Raman spectra were collected after 5 scans using a confocal spectrometer, with a magnification objective of 10x, corresponding to a spot size of 100 µm; acquisition time was 15 s. Fourier transform infrared spectroscopy was recorded in transmission mode after 100 scans, at a resolution of 4 cm^{-1} with an Equinox IFS55 spectrometer (Bruker) equipped with a DTGS detector. The pellets were made by diluting the samples in KBr (2 mg of sample for 200 mg of KBr), and then pressing them into self-supporting wafers using a hydraulic press (5-7.5 bar) for about 5 minutes. Atmospheric air spectrum has been used as a reference and subtracted from the showed spectra. Thermogravimetric analysis was performed on a thermo-analyzer Mettler Toledo TGA/SDTA 851 TA Instruments SDT 2960, in air (100 mL/min) from 25 to 900°C scanned at a heating rate of 10°C/min. X-ray photoelectron spectroscopy was carried out using an Axis Ultra (Kratos Analytical) spectrometer equipped with a 30° solid acceptance lens, a hemispherical analyser, and a monochromatic source of Al K_α (1486.6 eV) operated at 15 kV and 10 mA. The pressure within the analysis chamber was about 10^{-6} Pa. The angle between the surface normal and the axis of the analyser lens was 55°. The analysed area was approximately 1.4 mm^2 and the pass energy was set at 150 eV. In these conditions, the full

width at half maximum (FWHM) of the Au $4f_{7/2}$ peak of a clean gold standard sample was about 1.6 eV. A flood gun set at 8 eV and a nickel (Ni) grid placed 3 mm above the sample surface were used for charge stabilisation. The sample powder was pressed in small stainless steel troughs of 4 mm in diameter and placed on an aluminium conductive carousel. Before analysis, all samples were outgassed under vacuum (10^{-5} Pa) for 24 hours in order to remove physisorbates. The binding energy scale was calibrated taking the carbon C1s peak fixed at 284.8 eV (aliphatic component of carbon contamination) as reference. Atomic ratios were obtained using peak areas normalized on the basis of acquisition parameters and experimental sensitivity factors provided by the manufacturer. The Mn2p region was used to quantify Mn proportion. Proportions of lattice oxygen (structural, O_β) and chemisorbed oxygen (surface, O_α) were obtained by decomposing the O1s signal after deducing the oxygen-related to contamination carbon (O_γ). The Mn average oxidation state (AOS) was determined using the shift of the Mn3s binding energy [22, 23], following equation 1 [24].

$$AOS = 8.956 - 1.126\ \Delta E_s \quad (1)$$

Where ΔE_s represents the shift of the binding energy between Mn3s and its satellite. Nitrogen physisorption was carried out at -196°C using a Micromeritics Tristar 3000 in the relative pressure range [10^{-6}-0.99]. Before analysis, 150 mg of sample was outgassed at 150°C for 12 hours under primary vacuum. The specific area and pore size distribution were calculated using Brunauer-Emmett-Teller (BET) equation in the 0.05-0.30 P/P_0 range and the Barrett-Joyner-Halenda (BJH) method respectively. Error on the specific area was determined by calculating the standard deviation on a series of values related to 3 analyses of the same sample. The morphology was investigated using a LEO 983 GEMINI electron microscope operated at an acceleration voltage between 10 and 15 kV depending on the samples. Before analysis, the samples were metallized under argon atmosphere with an about 15 nm thick layer of chromium.

2.4 Catalytic performances

All the tests were carried out on Tartrazin Yellow (TY) as a representative azoïc organic dye used in many industries such as food, medicine, and cosmetics, and often found in their wastewaters. The molecular structure of TY is given on figure S_1. Standard catalytic tests were carried out in a batch reactor in the absence of light by wrapping the reactor with aluminium foil, and at room temperature (~25°C). They consisted in introducing 100 mL of TY solution (20 mg/L) into a 200 mL erlenmeyer, then adjusting the solution pH to 2.5 using H_2SO_4 (0.1M) or NaOH (0.1M), and introducing 50 mg of catalyst under magnetic stirring. At defined time intervals, about 2 mL of the reaction medium was withdrawn using a syringe, and then filtrated.

The residual concentration of TY was analysed at 425 nm with a GENESYS 10S Vis spectrophotometer. The bleaching degrees (%D) were calculated using equation 2.

$$\%D = [(C_0 - C_t) / C_0] \times 100 \quad (2)$$

Where C_0 and C_t represent initial and residual concentrations of TY at defined times.

In order to confirm a possible catalytic interaction between MnO_2 and dissolved oxygen, a TY solution has been evacuated of all the oxygen by a physical method, which consisted in bubbling nitrogen into the solution until the absence of remaining oxygen was checked with an OXY-4 oxygenometer, then the test was performed as described above. Moreover, bleaching and degradation processes of TY in the absence of radicals during the treatment were achieved using the catalyst alone, and adding n-butanol and KI as hydroxyls radical scavengers in the reaction medium. Finally, to gain deeper insights on the chemistry behind the bleaching/degradation process of TY, some HPLC analysis have been punctually carried out. This was achieved using an Empower 2 equipment, with a column Waters Xbrigde C18 4.6x50 mm 2.5µm. The chromatograms were recorded with the detector operating in the wavelength range 210-500 µm with a resolution of 1.2 nm. Moreover, chemical oxygen demand (COD) of different samples after the different catalytic treatments of TY has been followed by a colorimetric method. Precisely, using COD tubes (0-150 mg/L, Merck, 1.18751.0001), 2 mL of sample was introduced within the tube, mixed and heated for 2 hours at 148°C. The hot tube was cooled for 30 min at room temperature and analyzed by spectrophotometry. Also, recyclability tests of our best plasma-synthesized catalyst were conducted, as well as spectrophotometric analysis of the evolution of the concentration of Mn ions dissolved the reaction medium along a catalytic run (see Supporting Information).

3. Results and discussion

3.1. Evidence of the plasmachemical oxidation of Mn^{III} and reduction of Mn^{VII}

Figure 2 shows $Mn(CH_3COO)_3.2H_2O$ and $KMnO_4$ solutions before and after exposure to glidarc plasma respectively for 15 and 4.5 min. When the orange solution of manganese (III) acetate (Fig. 2a) or the purple solution of potassium permanganate (Fig. 2b) was exposed to the gliding arc discharge, their colour changes to black with apparition of precipitates. This

suggested that Mn^{III} and Mn^{VII} were respectively oxidized and reduced to what will indeed be proven later to be MnO_2.

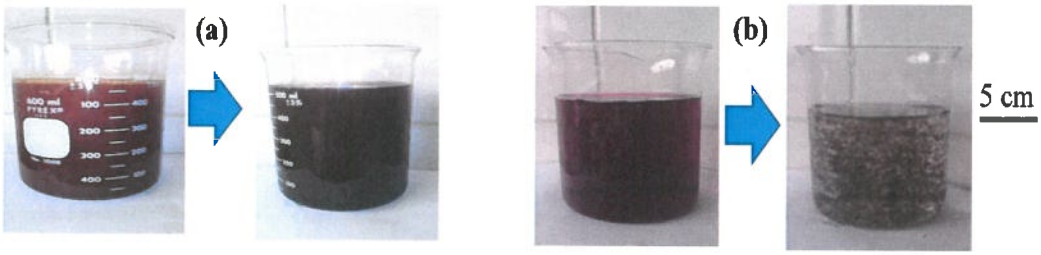


Fig. 2 Precursor solutions before (left) and after (right) exposure to the gliding plasma discharge (a: $Mn(CH_3COO)_3.2H_2O$; b: $KMnO_4$).

Moussa et al., Du et al., and Palwat et al. showed through emission spectroscopy analysis that hydroxyl ($HO^{\cdot}$) and nitrile ($NO^{\cdot}$) radicals are the major species generated within the gliding arc plasma when humid air is used as feeding gas [25, 26, 27]. In the case of $Mn(CH_3COO)_3.2H_2O$ solution, the plasmachemical oxidation would be induced by the $HO^{\cdot}$ radicals as shown by equations 3-5.

Half equations:

$$Mn^{3+}_{(aq)} + 2H_2O_{(l)} \rightarrow MnO_2(s) + 4H^+_{(aq)} + e^- \quad (E^0 = 0.95\ V) \qquad (3)$$

$$HO^{\cdot}_{(g)} + H^+_{(aq)} + e^- \rightarrow H_2O_{(g)} \quad (E^0 = 2.85\ V) \qquad (4)$$

Balance equation:

$$Mn^{3+}_{(aq)} + HO^{\cdot}_{(g)} + H_2O_{(l)} \rightarrow MnO_{2(s)} + 3H^+_{(aq)} \qquad (5)$$

The calculated thermodynamic equilibrium constant at 25°C is $K_1 = 10^{32}$, which indicates that the reaction is total and quantitative (Eq.5).

We could have expected the occurrence of the reduction of Mn^{3+} in Mn^{2+} through $NO^{\cdot}$ radicals (Eq. 6). Yet, calculating the thermodynamic equilibrium constant (K_2) of the reduction reaction we found 10^{28}. K_1 being largely higher than K_2 explains why the oxidation of Mn^{3+} by $HO^{\cdot}$ predominates.

$$3Mn^{3+}_{(aq)} + NO^{\cdot}_{(G)} + 2H_2O_{(l)} \rightarrow 3Mn^{2+}_{(aq)} + NO_3^-{}_{(aq)} + 4H^+_{(aq)} \qquad (6)$$

Moreover, exposing a Mn^{2+} solution to the glidarc discharge did not induce any precipitate in any acidic, neutral or basic medium.

As a counterpart, for the $KMnO_4$ solution, we witnessed a plasmachemical reduction, leading to the precipitation of $KMnO_4$. These events are induced by NO· radicals as described by equations (7-9).

Half equations:

$$MnO_4^-{}_{(aq)} + 4H^+{}_{(aq)} + 3e^- \rightarrow MnO_{2(s)} + 2H_2O_{(l)} \qquad (E° = 1.70\ V) \qquad (7)$$

$$NO^•{}_{(g)} + 2H_2O_{(l)} \rightarrow NO_3^-{}_{(aq)} + 4H^+{}_{(aq)} + 3e^- \qquad (E° = 0.94\ V) \qquad (8)$$

Balance equation:

$$MnO_{4(aq)} + NO^•{}_{(g)} \rightarrow MnO_{2(s)} + NO_3^-{}_{(aq)} \qquad (9)$$

The thermodynamic equilibrium constant (K_3) calculated for the reduction reaction (Eq.9) is very high 10^{38}, explaining the rapidity of the precipitation.

3.2 Materials characterization

3.2.1 Impact of gliding arc voltage

3.2.1.1 Structural analyses

The structure determination of the synthesized materials has been achieved by X-ray diffractometry (XRD) and vibrational spectroscopy. XRD (Fig 3) reveals that the material obtained by the reduction of Mn^{VII} has its crystal structure depending on the voltage at which it is produced. The XRD pattern of the material obtained by the reduction of $KMnO_4$ at high voltage (Fig.3a) corresponds to α-MnO_2 (cryptomelane, JCPDS 44-0141), whereas at LV (Fig.3b), δ-MnO_2 (K-birnessite, JCPDS 80-1098) is formed. Meanwhile, the plasmachemical oxidation of $Mn(CH_3COO)_3.2H_2O$ at HV (Fig.3c) led to γ-MnO_2 (nsutite, JCPDS 14-0644), and that performed at LV (Fig.3d) led to δ-MnO_2 (birnessite, JCPDS 80-1098). The nature of the MnO_2 polymorph obtained can thus be easily adjusted via the choice of the proper precursors used and voltage applied for the plasma.

A decrease of the voltage operated leads to a decrease of the amount of energy transferred from the electrical source to the molecules of the plasma gas, and to a decrease of the amount of reactive species produced. Correspondingly, at LV, longer nucleation times were recorded. Besides, the fact that the peak at 12.1° is missing in the diffraction pattern of δ-MnO_2 obtained from $Mn(CH_3COO)_3.2H_2O$ at LV (whereas this peak is present in the pattern of δ-MnO_2 obtained $KMnO_4$ at LV) is consistent with the absence (or presence) of potassium within the Mn precursor used. We should mention here that the solids characterized are the result of

several batches of plasma-precipitation that are mixed together. The fact that only one single polymorph (α-MnO_2, γ-MnO_2 or δ-MnO_2) is found for each of these samples attests the high reproducibility (from batch to batch) for each kind of syntheses.

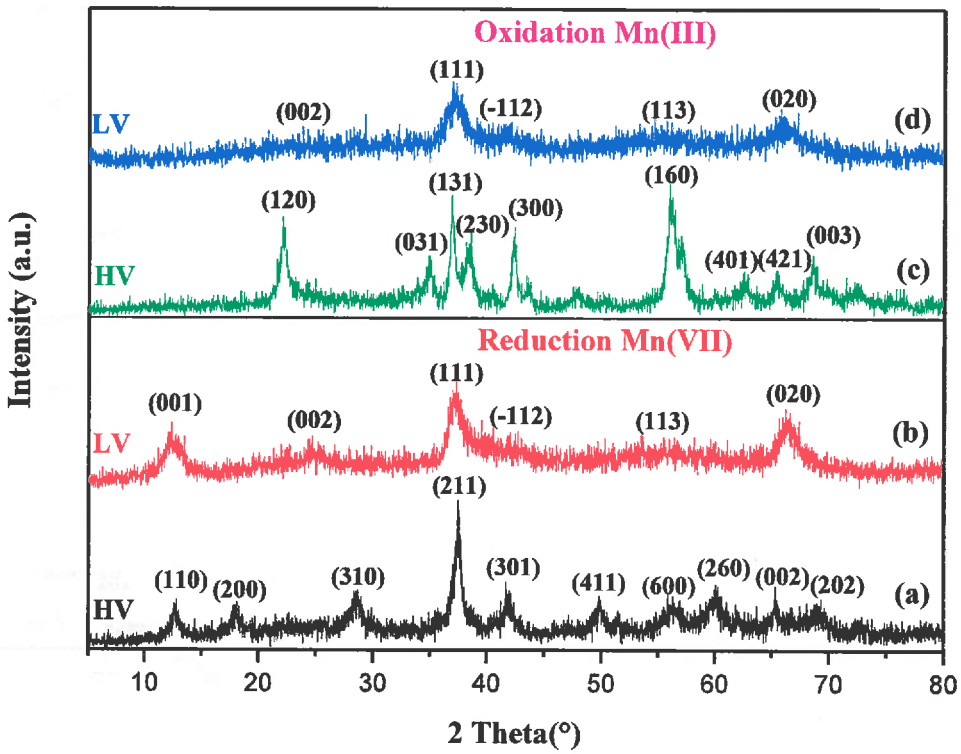


Fig. 3 XRD patterns of the plasma-synthesized MnO_2.

The Raman spectra of the four plasma-synthesized materials (Fig.4) confirmed their difference in structure. The sample obtained after reduction at HV (Fig.4a) shows three peaks at 391, 571 and 637 cm^{-1}. The weak peak at 391 cm^{-1} is assigned to Mn-O bending vibrations, and those at 571 and 637 cm^{-1} are ascribed to Mn-O-Mn stretching vibrations of MnO_6 octahedra within the (2x2) tunnels of the α-MnO_2 tetragonal structure [28]. The sample obtained by reduction at LV (Fig.4b) shows three main bands at 501, 557 and 640 cm^{-1}, featuring the symmetrical bending vibrations of Mn-O bond and basal plane made of octahedra sheets in δ-MnO_2 [29, 30]. The material obtained after oxidation at HV (Fig.4c) presents only two peaks at 339 and 632 cm^{-1} respectively ascribed to Mn-O bending and stretching vibrations of MnO_6 octahedra within the typical (1x2) tunnels of γ-MnO_2 orthorhombic structure [28, 31], while, that obtained at LV (Fig.4d) shows a single band at 640 cm^{-1}, which is ascribed to Mn-O bond vibrations within δ-MnO_2 polymorph [32]. Specifically, δ-MnO_2 obtained after reduction of $KMnO_4$ at LV shows two bands at 501 and 557 cm^{-1}, which do not appear on the spectrum of the δ-MnO_2 recovered after oxidation of $Mn(CH_3COO)_3.2H_2O$ at LV, and corroborates the XRD results in terms of

presence *vs* absence of K in the structures. Julien et al. reported that δ-MnO_2 is somehow unstable under the Raman laser beam and requires special care when analysed [33]. Analysis was thus carried out on eight points of each sample and revealed identical peaks positions, highlighting the homogeneity of the samples. The conclusions from the Raman analyses are further sustained by the FTIR spectra presented in Figure S_{2a}. In addition, the IR spectrum of α-MnO_2 obtained at HV shows an absorption band at 1380 cm^{-1} more intense than those of the three other MnO_2. This reflects the significantly more intense presence of crystallization or structural water within the α-MnO_2 polymorph. This more important quantity of structural water in α-MnO_2 was confirmed by thermogravimetric analysis (Fig.S_{2b}).

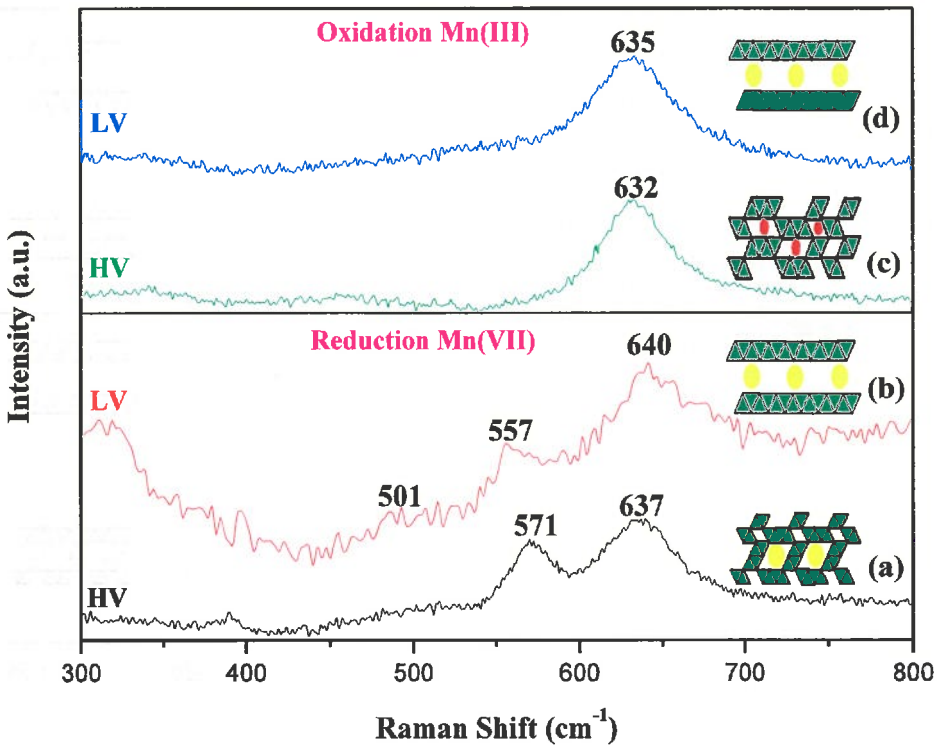


Fig. 4 Raman scattering spectra of the synthesized MnO_2. The insets are the crystal representation of each polymorph (red balls: H_2O; yellow balls: K^+ and H_2O).

3.2.1.2. Surface and morphology analyses

The surface composition of the four plasma-synthesized MnO_2 and their Mn average oxidation state (AOS) have been determined by XPS. Figure 5 depicts the survey spectrum of each sample, displaying Mn3p, Mn3s, C1s, O1s, Mn2p, and Mn2s peaks; the K1s peak was also observed for the two samples obtained from $KMnO_4$ via the plasma reduction route. The measured surface compositions for each material are summarized in table 1. The spin energy separation value between $Mn2p_{1/2}$ and $Mn2p_{3/2}$ peaks (Fig.S_{3a}) within each material is in accordance with the data of $Mn2p_{1/2}$ and $Mn2p_{3/2}$ in MnO_2 [24, 34]. Because of the complexity

of decomposing the Mn 2p area when dealing with a mixture of various Mn oxidation states [35], and thus the weak low accuracy of the corresponding distributions that may be estimated, the AOS values were calculated from the Mn3s and its satellite region [22-24] (Fig. S_{3b}). This reveals the presence of Mn in each sample in a mixture of Mn(III) and of Mn(IV). Table 1 additionally shows the proportions of the different oxygen components in each material, considering lattice oxygen (O_β) falling in the binding energy range of 529.7-530.1 eV, and chemisorbed surface oxygen (O_α) falling in the range of 531.3-531.9 eV (Fig.S_4) [36, 37]. The oxygen contribution related to contamination carbon (O_γ) falling in the range 532.4-533.2 eV [36, 37], was calculated from the corresponding contributions found in the C1s signal. δ-MnO_2 (Oxi/LV) shows a higher density of chemisorbed oxygen (O_α) at its surface than the three other materials, which suggests a higher surface oxidation capacity for this material. More generally, more O_β is found for both MnO_2 obtained via plasma-reduction than for those obtained via plasma-oxidation.

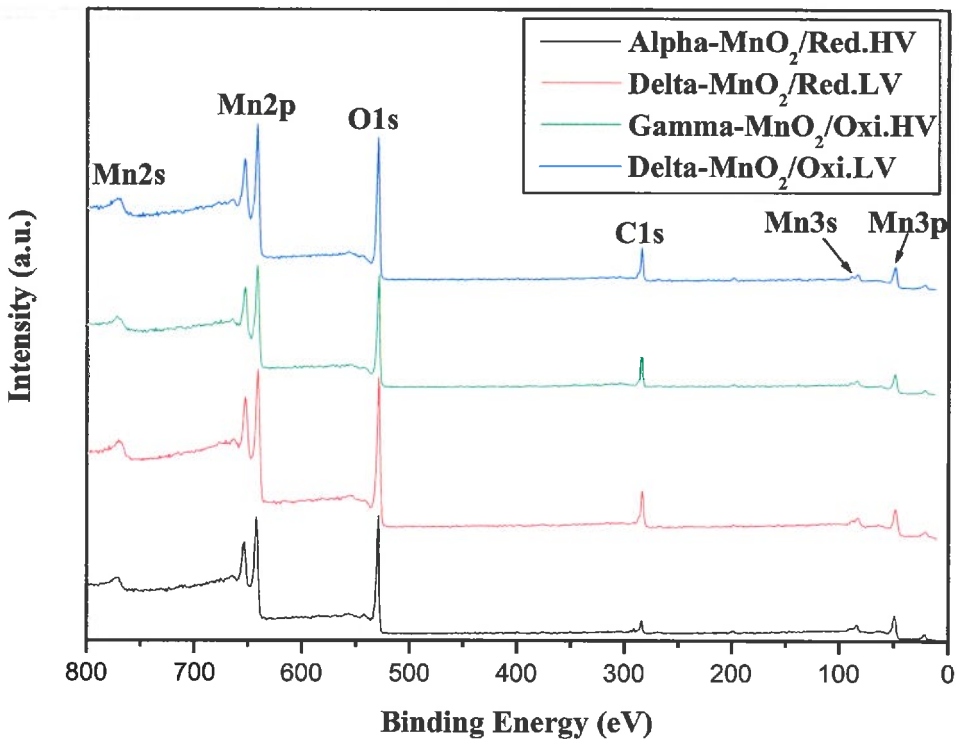


Fig. 5 XPS survey spectra of plasma-synthesized MnO_2.

Table 1 XPS data of plasma-synthesized MnO_2.

Sample	%C1s	%K	%Mn	%Otot	O_α/O_β	ΔMn2p (eV)	ΔMn3s (eV)	AOS (Mn)
α-MnO_2 Red/HV	21.8	1.0	23.1	54.1 of which $O_\gamma = 4.9$ $O_\alpha = 6.8$ $O_\beta = 42.4$	0.16	11.6	4.75	3.61
δ-MnO_2 Red/LV	31.4	0.4	17.8	50.4 of which $O_\gamma = 6.6$ $O_\alpha = 3.9$ $O_\beta = 39.9$	0.10	11.3	5.09	3.22
γ-MnO_2 Oxi/HV	32.0	0	20.0	48.0 of which $O_\gamma = 5.7$ $O_\alpha = 6.6$ $O_\beta = 35.7$	0.18	11.3	4.82	3.53
δ-MnO_2 Oxi/LV	27.8	0	19.2	53.0 of which $O_\gamma = 7.3$ $O_\alpha = 8.8$ $O_\beta = 36.9$	0.24	11.4	5.09	3.22

The material obtained by reduction of $KMnO_4$ at HV (Fig.6a) shows interwoven nanorods, with diameters in the range 30-45 nm and length in the 200-400 nm range, while that obtained at LV (Fig.6b) reveals nanosheets. The material obtained by oxidation of $Mn(CH_3COO)_3.2H_2O$ at HV (Fig.6c) shows nanospheres with diameter in the range 60-100 nm and that obtained at LV shows nanoflakes. A variation of the morphology of the samples is thus recorded when the voltage applied during the plasma-precipitation was varied. Besides, nanosheets and nanoflakes obtained at LV (Fig.6d) are in concordance with the typical morphology of both δ-MnO_2 polymorphs as revealed by XRD analysis.

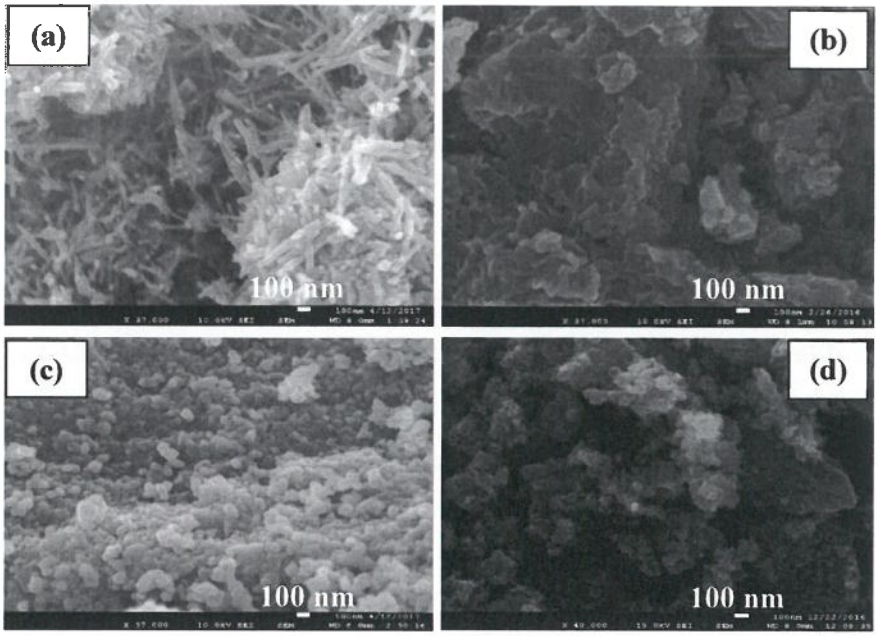


Fig. 6 SEM images of the plasma-synthesized materials: (a) α-MnO_2.Red.HV, (b) δ-MnO_2.Red.LV, (c) γ-MnO_2.Oxi.HV, (d) δ-MnO_2.Oxi.LV.

3.2.1.3. Textural analyses

The adsorption-desorption isotherms of the four plasma-synthesized MnO_2 are depicted on Figure 7. These isotherms show a hysteresis loop in the relative pressure range 0.5-1, which is typical of type IV isotherms observed for mesoporous materials [38]. The mesopores might here likely be seen as the spaces between nanorods, nanosheets and nanospheres as revealed by SEM. A shift to higher relative pressure of the hysteresis loop is observed for γ-MnO_2, which illustrates an adsorption process within larger pores than those of α-MnO_2. The δ-MnO_2 obtained after the reduction of $KMnO_4$ at LV, does not show capillary condensation at the adsorption, but a sudden capillary decondensation is seen, which suggests the presence of slit pores, quite homogeneous in size, likely between the sheets observed in SEM [39, 40]. In comparison, δ-MnO_2 obtained after the oxidation of $Mn(CH_3COO)_3.2H_2O$ at LV, shows a adsorption isotherm without apparent capillary condensation event, a hysteresis loop very narrow and spread over a large range of relative pressure between 0.45 and 1.0. This attests the presence of slit pores with more dispersity in their size than observed for δ-MnO_2 obtained after the reduction of $KMnO_4$ at LV, and fits with the less regular shapes and sizes of the corresponding flakes. The hysteresis "in two parts" of the γ-MnO_2 obtained by oxidation at HV suggests some size bimodality in a population made of large pores (hysteresis at relatively high

relative pressure), and much diverse in size (hysteresis spreading over a large range of relative pressure).

Table 2 reveals an increase of the specific surface area with the decrease of the voltage during plasmachemical synthesis via reduction or oxidation. This increase could be ascribed to the longer nucleation time needed at LV (as due to a lower availability of reducing NO· or oxidizing HO· species), favoring a more important development of pores in the materials. The higher specific area of both δ-MnO_2 than those of α-MnO_2 and γ-MnO_2 could be ascribed to the larger distance between sheets in δ-MnO_2 polymorph (7Å) likely able to better adsorb nitrogen molecules (3.53Å) compared to the tunnels of α-MnO_2 (4.6Åx4.6Å) and γ-MnO_2 (1.89Åx4.6Å) [36].

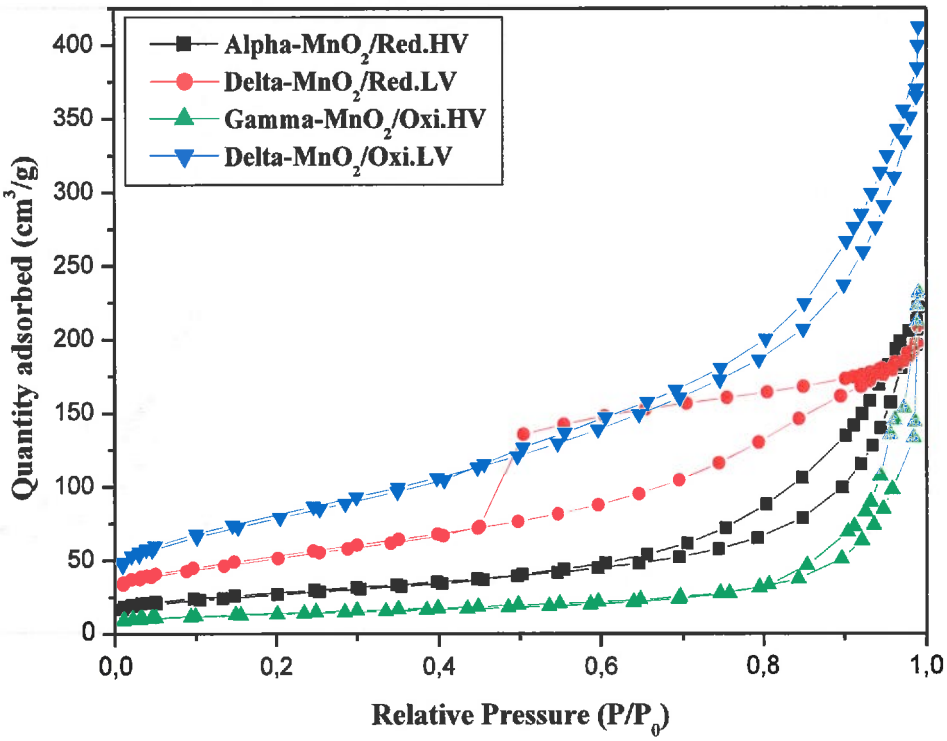


Fig. 7 Adsorption-desorption isotherms of plasma-synthesized MnO_2.

Table 2 Nitrogen physisorption data of plasma-synthesized MnO_2 at different voltages.

	Surface area (m^2/g)	**Average pore size (nm)**	**Pore volume (cm^3/g)**
α-MnO_2 (Red/HV)	98 ± 7	12	0.33
δ-MnO_2 (Red/LV)	186 ± 13	5	0.31
γ-MnO_2 (Oxi/HV)	48 ± 3	29	0.34
δ-MnO_2 (Oxi/LV)	289 ± 20	8	0.56

3.2.2 Impact of gliding arc plasma airflow

Figure 8a depicts X-ray diffraction patterns of materials obtained after plasmachemical reduction of $KMnO_4$ at HV at different airflow values. The material obtained at 800 L/h shows diffraction peaks typical of the α-MnO_2 polymorph (JCPDS 44-0141), whereas, that obtained at 600 L/h shows the peaks typical of the δ-MnO_2 polymorph (K-birnessite, JCPDS 80-1098). The difference of nature of the polymorph obtained at the difference airflows applied, would be related to the corresponding difference in the amount of reducing species ($NO^{\cdot}$) generated in the plasma. Precisely, at 600 L/h, the amount of such species is less than that at 800 L/h, therefore inducing a longer nucleation time, and a different corresponding polymorph than that obtained at higher flow. Raman scattering spectra of both materials (Fig.8b) confirm that α-MnO_2 and δ-MnO_2 polymorphs were obtained respectively at 800 and 600L/h. Figure 9 shows SEM images of both materials, and reveals nanorods and nanosheets respectively at 800 (Fig.9a) and 600L/h (Fig.9b). Textural data are summarized on table 3. An increase of the specific area is observed with the decrease of the airflow, which could be ascribed to the fact that the longer synthesis time required at low airflow favors a significantly more important development of pores in the precipitated material. There is a clear parallelism between the effect induced by working at LV (rather than at HV, see section 3.2.1), and by working at low airflow: both approaches, corresponding to less plasma species generated, thus longer nucleation time, with less crystallinity and a more expanded texture (higher specific surface area and smaller mesopores).

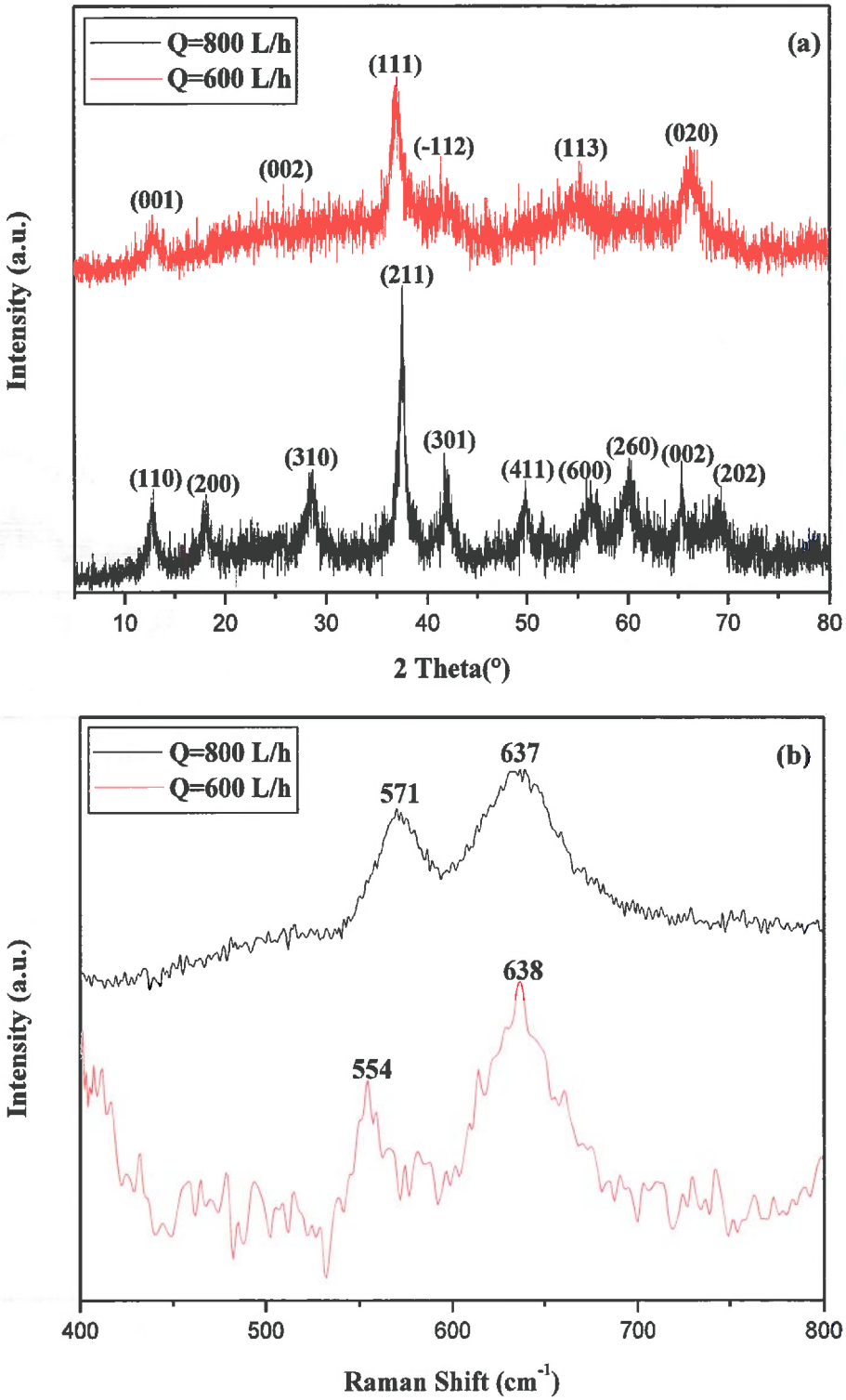


Fig. 8 XRD patterns (a) and Raman spectra (b) of plasma-synthesized MnO_2 prepared at 600 and 800L/h, HV.

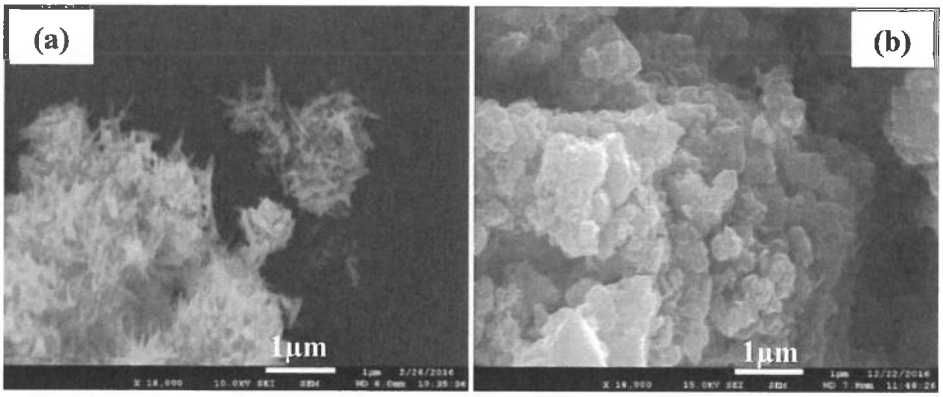


Fig. 9 SEM images of plasma-synthesized MnO_2 prepared at (a) 800 and (b) 600L/h, HV.

Table 3 Nitrogen physisorption data of plasma-synthesized MnO_2 at different airflows, HV

	Surface area (m^2/g)	**Average pore size (nm)**	**Pore volume (cm^3/g)**
α-MnO_2 (800L/h)	98 ± 7	12	0.33
δ-MnO_2 (600L/h)	174 ± 12	9	0.47

3.3 Catalytic bleaching/degradation of Tartrazin Yellow (TY)

The bleaching degrees of Tartrazin Yellow (TY) with four plasma-synthesized α-MnO_2 (Red/HV/800 L/h), δ-MnO_2 (Red/LV/800 L/h), γ-MnO_2 (Oxi/HV/800 L/h) and δ-MnO_2 (Oxi/LV/800 L/h) are depicted in Fig 10. Correspondingly, bleaching degrees of 96, 97, 71 and 96% were obtained after 180 min of treatment. It appears that, each catalyst used alone displays an efficient bleaching of TY. We would have expected a more intense bleaching of TY with δ-MnO_2 (Oxi/LV) than those with the three other materials, because of its higher ratio O_α/O_β and specific surface area. As this is not the case, these results mean that the performances are not only dictated by these two last parameters, but that they are also dictated by the crystalline structure of the catalysts. At this stage, only speculation can be proposed to account for this but a possibility is that it is due to the different pore sizes of the compared materials, either at the mesoscopic level (α-MnO_2 has larger mesopores than δ as shown in Table 3, which could make that the TY molecules diffuse and react more easily in α than in δ) or a more atomic scale (the tunnels typical of the α polymorph being more prone to allow reactive oxygen species to be transferred and/or activated than the lamellar structure of δ is).

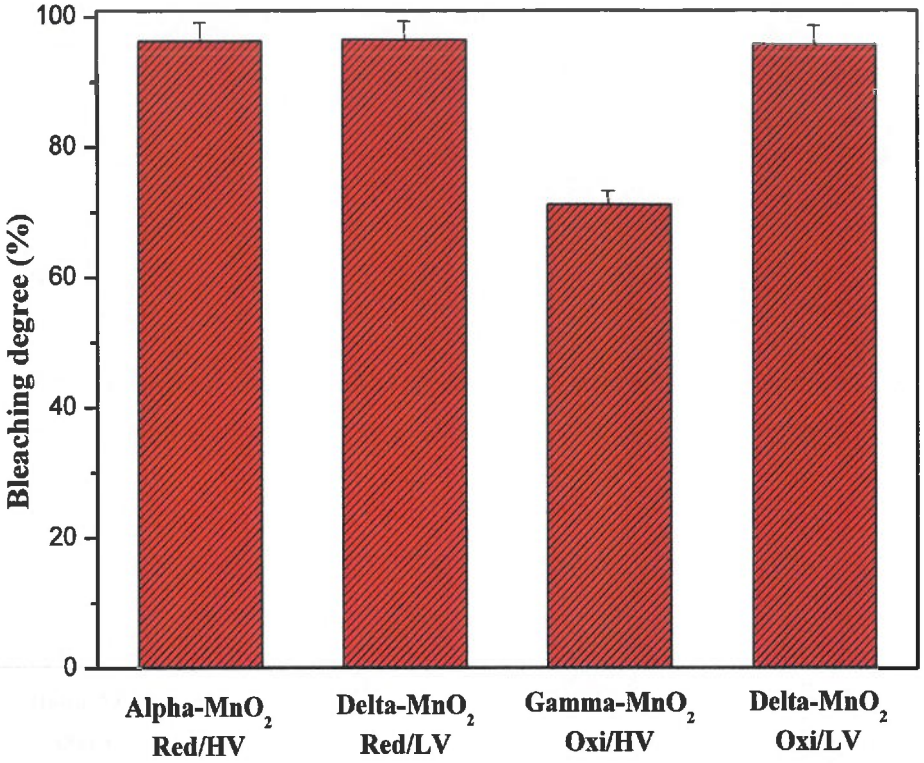


Fig. 10 Bleaching degrees of TY with four MnO_2 obtained at different voltages, 800 L/h.

In order to investigate whether the colour removal during the catalytic treatment was not only due to a simple adsorptive removal of TY by the solid materials, α-MnO_2 (Red/HV) was recovered after almost complete bleaching of TY, dried, and introduced in distilled water at pH 7 (first experiment) and 10 (second experiment). These pH values are unfavourable for the adsorption of TY on MnO_2. Indeed, on one hand one may consider that at these pH values the TY is negatively charged (the two sulfonic plus the carboxylic acid moieties are all three deprotonated, *vs* the sole azo moeity is protonated), and on the other hand isoelectric point of MnO_2 is 4.4 making it negatively charged as well. Overall, it means that at both pH 7 and 10 the two players are both negatively charged and should repulse each other. Hence if a given TY quantity had been adsorbed on the catalyst surface during the initial step of the experiment, it should here desorb intact and leach in the medium. Along stirring, samples of the liquid were taken at different time intervals and analysed. A slight increase of the concentration of TY within the first minutes of this desorption experiment was observed (Fig.11a). However, the concentration of TY measured in the desorption medium at both pH, stabilized very quickly to a low value as compared to the concentration of TY introduced at the beginning of the bleaching test. The small quantity of TY desorbed likely corresponds to the few molecules of TY that remain at the surface of the catalyst when the bleaching tests was interrupted, but may not

account for the much bigger amount of TY having "disappeared" during the bleaching test. All in all, this suggests that during the bleaching experiments TY is not only adsorbed on the catalyst but it also undergoes a real decomposition after its adsorption. This claim is further supported by the FTIR spectrum of the catalyst after the reaction (Fig.11b). Indeed if all the TY having been consumed along the bleaching test had simply adsorbed on the catalyst surface, such huge amount of TY should lead to the observation of its fingerprint IR absorption peaks in the spectrum of the catalyst after bleaching. Yet our such IR analysis did not show any other peaks than those present on the spectrum of the fresh catalyst. Besides, we observe the decrease in intensity of the absorption band around 1382 cm^{-1} on the α-MnO_2 spectrum after treatment (Fig.11b); this could be attributed to the removal of structural or chemisorbed water from the (2x2) and (1x1) tunnels of this polymorph [28] after adsorption and decomposition of the pollutant.

The evolution of the UV-Vis spectrum of TY solution along the catalytic treatment (α-MnO_2) is shown on Fig S_5. Besides the fact that the two bands of TY (425 and 258 nm) vanish with the time of reaction, as exploited to calculate the conversions / degrees of bleaching, no other band does grow at any wavelength. This suggests that the bleaching corresponds to more than a simple cleavage of the TY molecule in smaller molecules (for example at the –N=N– moiety level) that would make it loose its color, and that a deeper degradation/oxidation of the polyaromatic rings eventually occurs [41, 42]. The data in table S_1 confirm this eventuality as revealing a partial decrease of the chemical oxygen demand (COD) after 180 min of catalytic treatment of TY with α-MnO_2, illustrating that a partial mineralization of TY occurred. Figure S_6 shows HPLC chromatograms of TY solution before and after treatment. A significant decrease of the TY peak (t_r=0.732 min) is already visible after 30 min of treatment; the peak reaches a negligible value after 120 min of treatment and is totally vanished after 180 min. More than this, one should also draw the attention on the fact that no new peak does appear on the HPLC chromatogram recorded until more than 7 min of retention time, whereas if the bleaching of TY was due to its scission in for example two parts, one could have expected a new signal. This result once again highlights the occurrence of a deep degradation of TY during the catalytic process.

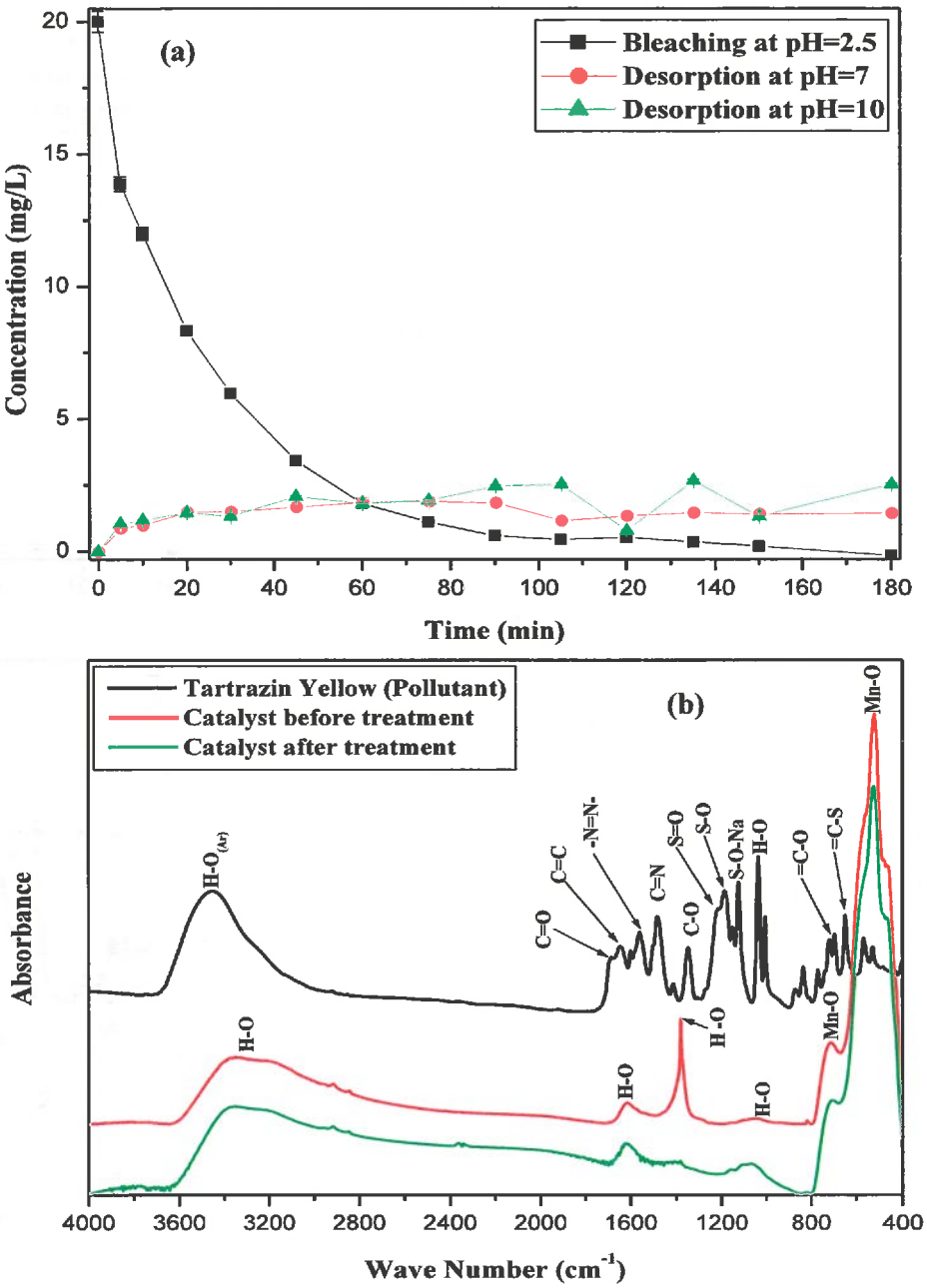


Fig. 11 (a) Evolution of concentration during TY bleaching with the catalyst alone and desorption tests, (b) FTIR spectra of TY and α-MnO_2 (Red/HV) catalyst before and after used.

The results of Fig. 11 are obtained with α-MnO_2, but the same were also obtained for the three other MnO_2 materials synthesized (not shown). These results allow hypothesizing that, all plasma-synthesized MnO_2 with Mn in a mixed valence (III, IV), are able to catalyse the oxidative degradation of organic molecules. In fact, it has been shown that such materials in

addition to having vacant oxygen sites (activation sites), have the ability to release electrons which can further react with dissolved oxygen and water by ionisation and dissociation respectively, thus producing powerful oxidizing species such as $HO^{\cdot}$, and $HO_2^{\cdot}$ radicals (see corresponding set of chemical equations on Fig.S_7) [43, 44, 45]. These oxidizing species would then contribute to the bleaching of the pollutant. Wu et al. reported that the presence of K^+ as doping element within α-MnO_2, generates structural defects (vacant oxygen in the lattice), which may be the active sites during the catalytic reaction [46]. Hernandez et al. show that the presence of chemisorbed oxygen (O_α) at the surface of α-MnO_2 may be related to the dynamics of the vacant oxygen sites, which defects would interact with dissolved oxygen and water molecules, leading to the formation of $HO^{\cdot}$ and $HO_2^{\cdot}$ [47]. To confirm the possible contribution of dissolved oxygen in such process, we performed a comparison between the bleaching of TY with oxygenated *vs* deoxygenated reaction medium (Fig. S_8). Such deoxygenation induced a marked decrease of the bleaching efficiency. This was observed for the four MnO_2 and confirms the hypothesis that there is a significant need of dissolved oxygen for the bleaching of TY with the MnO_2 catalyst (Fig. S_8). Such result corroborates that obtained by Xiao et al. who showed that α-MnO_2 with Mn in a mixed valence (III, IV) synthesized by a reflux method, can indeed degrade effectively ciprofloxacin in solution without any input of oxidizing agent as hydrogen peroxide for example [48].

Table S_2 summarizes XPS data for one of the catalysts (α-MnO_2, HV/Red) before and after having been used for the bleaching of TY with both the pristine (ie still containing dissolved molecular oxygen) and deoxygenated reaction medium. A significant increase of the chemisorbed oxygen (O_α) contribution is observed with the pristine reaction medium, which could be ascribed to water oxygen having chemically settled on the catalyst during the treatment. At the same time, a decrease of the lattice oxygen (O_β) concentration after catalysis is noted with both reaction media. The decrease of the oxygen lattice (O_β) concentration is however higher with the deoxygenated reaction medium than with the pristine one. This indicates the occurrence of a partial consumption of oxygen from the catalyst lattice during the catalytic process in the absence of dissolved molecular oxygen. This result is supported by the decrease of AOS recorded for Mn after the catalytic degradation of TY in such oxygen-free conditions. Finally, to further prove that the degradation of TY also proceeds via the involvement of hydroxyl radicals ($HO^{\cdot}$), n-butanol and KI have been used as scavengers of these species [49-55]. Fig 12 displays the bleaching degree of TY after 180 minutes of reaction with the four MnO_2 in the presence and absence of n-butanol and KI. A decrease of the

bleaching efficiency is recorded when either n-butanol or KI was added during the treatment of TY. These results highlight that the degradation of TY is indeed at least partially due to hydroxyl radicals generated by the catalysts (Fig.S7). The higher hydroxyl scavenging effect observed with KI than with n-butanol, despite the huge difference in concentration used, can be related to the higher rate constant of the reaction of the hydroxyl radical with KI (Eq.10) than with n-butanol (Eq.11) [50, 52].

$$I^- + HO^\cdot \rightarrow I^\cdot + HO^- \qquad K_1 = 1.2\times10^{10}\ M^{-1}.S^{-1} \qquad (10)$$

$$t\text{-BuOH} + HO^\cdot \rightarrow t\text{-BuO}^\cdot + H_2O \qquad K_1 = 6\times10^{8}\ M^{-1}.S^{-1} \qquad (11)$$

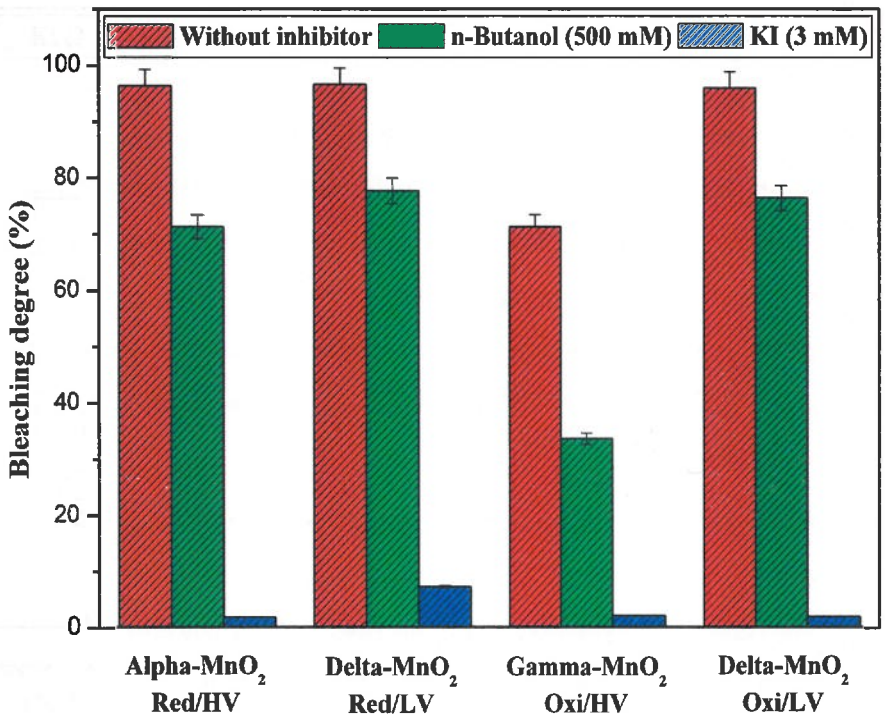


Fig. 12 Hydroxyl radicals scavengers effect during treatment of TY with each catalyst.

Finally, the recyclability and stability have been evaluated for the best of our plasma synthesized materials, namely α-MnO_2 (for more details, see Supporting Information). It proved to be recyclable along 4 successive catalytic tests (Figure S9). In addition, we have evaluated the evolution of the concentration of Mn in the reaction medium along the first test, using a spectrophotometric method. The catalyst leaches a small amount of Mn within the 5 first minutes of test, but then it remains stable (as the concentration of Mn then remained stable as after the first 5 minutes of test, Figure S9). From this, we concluded (i) the high catalytic stability of the material, and (ii) a low leaching of Mn during the catalytic process.

Conclusion

Mesoporous α-MnO_2 (Red/HV), δ-MnO_2 (Red/LV), γ-MnO_2 (OXi/HV) and δ-MnO_2 (OXi/LV) colloids were successfully plasma-synthesized after exposure of $KMnO_4$ and $Mn(CH_3COO)_3.2H_2O$ as precursors to gliding arc plasma operated at high (HV) and low (LV) voltages. This study reveals that the crystalline structure, the morphology and the texture of the oxides obtained depend markedly on the voltage applied and the airflow to generate the plasma. Precisely an increase of specific surface area was observed when a lower voltage was applied. The same effect was also recorded, when the airflow applied was low. The catalytic tests revealed an efficient bleaching of Tartrazin Yellow (TY) for each of the catalysts prepared. The bleaching is proved not to be due to a simple adsorption of the dye on the solids but to its true degradation, at least partially corresponding to its mineralization. The catalysts were active as they were able to activate O_2 dissolved in the water likely thanks to their structure based on a mixed Mn^{III}/Mn^{IV} valence. The best of our plasma-precipitate material, namely α-MnO_2, proved to be recyclable, maintaining its bleaching ability up to four successive runs, and quasi not undergoing any dissolution under the catalytic conditions. Overall, gliding arc plasma thus appears as an easy and effective synthesis device of MnO_2 nanostructures. The technique is in addition very versatile as changing simple parameters as the nature of the precursor used, or the voltage and airflow used to generate the plasma allows obtaining at wish all the various polymorphs of MnO_2 without difficulty and with interesting textural features.

Acknowledgements

The authors are grateful to Prof. J.-L. Brisset (University of Rouen) rest in peace and S. Nzali (University of Dschang) for the plasma reactor and pollutant supply respectively. They are also grateful to Antoine Tiya-Djowe (from University of Yaounde I, currently in University of Bordeaux), Georges Kamgang-Youbi, Elie Acayanka (from University of Yaounde I) for advices in the writing of the draft. The authors finally thank the "Université catholique de Louvain" for the scholarship awarded to F.W. Boyom Tatchemo in the frame of "Coopération au développement" doctoral program.

References

1. Y.-S. Ding, X.-F. Shen, S. Sithambaram, S. Gomez, R. Kumar, V.M.B. Crisostamo, S.L. Suib, M. Aindow, Chem. Mater, 17 (2005) 5382-5389.
2. H.Y. Lin, Y.P. Sun, B.J. Weng, C.T. Yang, N.T. Suen, K.H. Liao, Y.C. Huang, J.Y. Ho, N.S. Chang, H.Y. Tang, Electrochim. Acta, 52 (2007) 6548-6553.

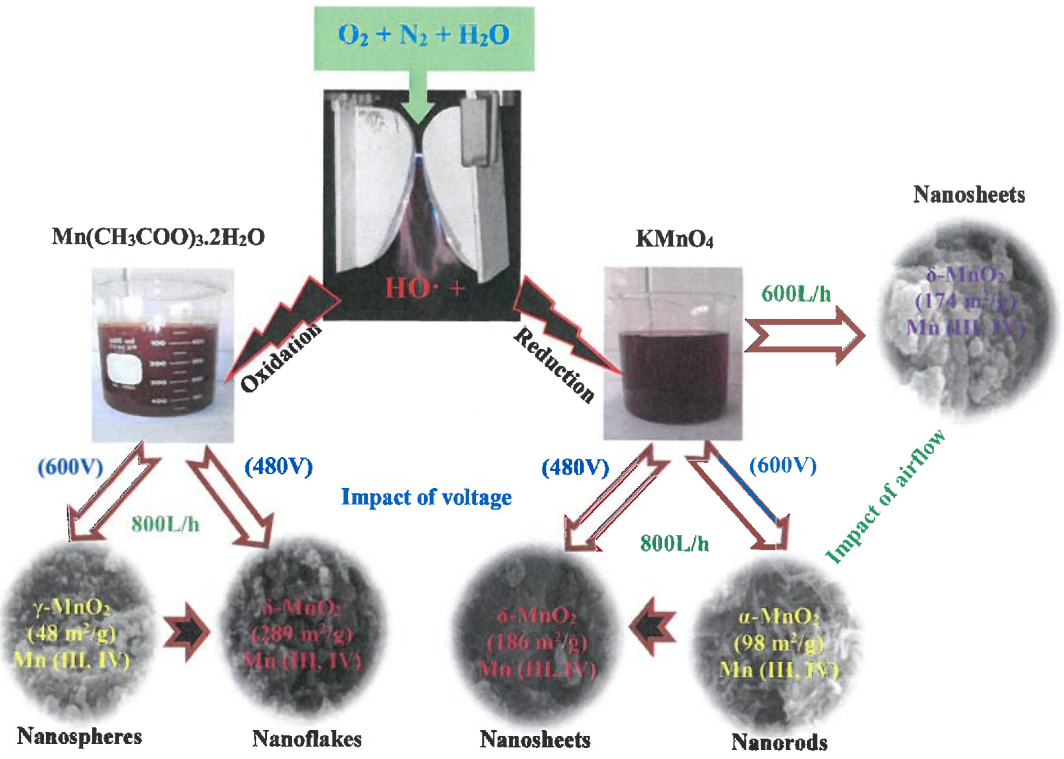
3. W.Y. Hernandez, M.A. Centeno, F. Romero-Sarria, S. Ivanova, M. Montes, J.A. Odriazola, Catal. Today, 157 (2010) 160-165.
4. M. Panahi-Kalamuei, K. Motevalli, M. Aliabadi, J. Mater. Sci. Mater. Electron. 27 (2016) 4631-4635.
5. A.H. Gemeay, R.G. El-Sharkawy, I.A. Mansour, A.B. Zaki, Appl. Catal. B 80 (2008) 106-115.
6. Y.-L. Chan, S.-Y. Pung, S. Sreekantan, F.-Y. Yeoh, J. Exp. Nanosci. 11:8 (2016) 603-618.
7. W.-H. Ryu, D.-W. Han, W.-K. Kim, H.-S. Kwon, J. Nanopart. Res. 13:10 (2011) 4777-4784.
8. L. Zhang, Z.-H. Liu, X. Tang, J. Wang, K. Ooi, Mater. Res. Bull. 42 (2007) 1432-1439.
9. X. Liu, C. Chen, Y. Zhao, B. Jia, J. Nanomater. (2013) 736375,7.
10. X.-W. Liu, X.-F. Sun, Y.-H. Huang, G.-P. Sheng, K. Zhou, R.J. Zeng, F. Dong, S.-G. Wang, A.-W. Xu, Z.-H. Tong, H.-Q. Yu, Water Res. 44 (2010) 5298-5305.
11. E.K. Nyutu, C.-H. Chen, S. Sithambaram, V. Mark, B. Crisostomo, S.L. Suib, J. Phys. Chem. C 112 (2008) 6786-6793.
12. S.H. Kim, S.J. Kim, S.M. Oh, Chem. Mater. 11 (1999) 557-563.
13. J.L. Liu, L.Z. Fan, X. Qu, Electrochimi. Acta 66 (2012) 302-305.
14. X. Li, B. Wei, Nano. Energy (2012) 1479-487.
15. Y. Li, J. Wang, Y. Zhang, M.N. Banis, J. Liu, D. Geng, R. Li, X. Sun, J. of Colloid Interface Sci. 369 (2012) 123-128.
16. M.A. Bratescu, N. Saito, O. Takai, Curr. Appl. Phys. 11 (2011) 30-34.
17. A. Doubla, S. Laminsi, S. Nzali, E. Njoyim, J. Kamsu-Kom, J.-L. Brisset, Chemosphere 69 (2007) 332-337.
18. B. Benstaali, D. Moussa, A. Addou, J.-L. Brisset, Eur. Phys. J. Appl. Phys. 4 (1998) 171-179.
19. E. Acayanka, A. Tiya.Djowe, S. Laminsi, C.C. Tchoumkwe, S. Nzali, A. Poupi Mbouopda, P.T. Ndifon, E.M. Gaigneaux, Plasma Chem. Plasma Process. 0272-4324, 33 (2013) 725-735.
20. A. Tiya-Djowe, S. Laminsi, G.L. Noupeyi, E.M. Gaigneaux, Appl. Catal., B 176 (2015) 99-106.
21. F.W. Boyom-Tatchemo, S. Nzali, G. Kamgang-Youbi, A. Tiya-Djowe, D. Kuete-Saa, E. Acayanka, S. Laminsi, E.M. Gaigneaux, Top. Catal, (2017) DOI 10.1007/s11244-017-0761-9.

22. C.M. Cellier, V. Vromman, V. Ruaux, E.M. Gaigneaux, P. Grange, J. Phys.Chem. B 108 (2004) 9989-10001.
23. C. Cellier, S. Lambert, E.M. Gaigneaux, C. Poleunis, V. Ruaux, P. Eloy, C. Lahousse, P. Bertrand, J.-P. Pirard, P. Grange, Appl. Catal., B (2007) 406-416.
24. C. Liu, J. Wang, L. Xiang, J. Nanomater. (2013) 389634, 4.
25. D. Moussa, H. Vitrac, B.G. Cheron, E. Hnatiuc, A. Addou, J.-L. Brisset, Plasma Physics and Fusion Technology 6:34 (2002) 34009462.
26. C.M. Du, J.H. Yan, IEEE T. Plasma. Sci. 35:6 (2007) 1648-1650.
27. J. Pawlat, P. Terebun, M. Kwiatkowski, B. Tarabova, Z. Kovalova, K. Kucerova, Z. Machala, M. Janda, K. Hensel, Plasma Chem Plasma Process. (2019 1-16.
28. M. Sun, B. Lan, L. Yu, F. Ye, W. Song, J. He, G. Diao, Y. Zheng, Mater. Lett. (2012) 18-20.
29. Y. Li, J. Wang, Y. Zhang, M.N. Banis, J. Liu, D. Geng, R. Li, X. Sun, J. colloid Interface Sci., 369 (2012) 123-128.
30. C. Julien, M. Massot, R. Baddou-Hadjean, S. Franger, S. Bach, J.P. Pereira-Ramos, Solid State Ion., 159 (2003) 345-356.
31. C.M. Julien, M. Massot, Bulg. Acad. Sci. (2004) 1-17.
32. A.K. Sinha, M. Pradhan, T. Pal, J. Phys. Chem. C, 117 (2013) 23976-23986.
33. C.M. Julien, M. Massot, C. Poinsignon, Spectrochim. Acta A, 60 (2004) 689-700.
34. F. Xiao, Y. Xu, J. Mater. Sci.- Mater. Electron, (2012) 10854-012-1034-9.
35. M.C. Biesinger, B.P. Payne, A.P. Grosvenor, L.W.M. Lau, A.R. Gerson, R.S.C. Smart, Appl. Surf. Sci. 257 (2011) 2717-2730.
36. H. Lin, D. Chen, H. Liu, X. Zou, T. Chen, Aerosol and Air Qual. Res., 17 (2017) 1011-1020.
37. Y. Peng, H. Chang, Y. Dai, J. Li, Procedia.Environ.Sci (2013), 18, 384-390.
38. S. Zhu, X. Wang, W. Huang, D. Yan, H. Wang, D. Zhang, J. Mater. Res. 21:11 (2006) 2847-2854.
39. N. Subramanian, B. Viswanathan, T.K. Varadarajan, RSC Advances, 4 (2014) 33911.
40. M.-S. Song, K.M. Lee, Y.R. Lee, I.Y. Kim, T.W. Kim, J.L. Gunjakar, S.-J. Hwang, J. Phys. Chem. C (2010), 114, 22134-22140.
41. N. Modirshahla, A. Hassani, M.A. Behnajady, R. Rahbarfam, Desalination 271 (2011) 187-192.
42. M.A. Behnajady, N. Modirshahla, R. Hamzavi, J. Hazard. Mater. B 133 (2006) 226-232.

43. S. Sultana, Z. Ye, S.K.P. Veerapandian, A. Lofberg, N.D. Geyter, R. Morent, J.M. Giraudon, J.F. Lamonier, Catal Today. (2018), 307, 20-28.
44. T. Zhu, Y.D. Wan, Y.Q. Jin, Int. J. Environ. Sci. Technol. 8 : 3 (2011) 621-630.
45. T. Sriskandakumar, N. Opembe, C.-H. Chem, A. Morey, C.K. Ondu, S.L. Suib, J. Phys. Chem. A 113 (2009) 1523-1530.
46. Y. Wu, R. Feng, C. Song, S. Xing, Y. Gao, Z. Ma, Catal Today. (2017) 500-506.
47. W.Y. Hernandez, M.A. Centeno, S. Ivanova, P. Eloy, E.M. Gaigneaux, J.A. Odriozola, Appl Catal B 123-124 (2012) 27-35.
48. X. Xiao, S.-Sun, M.B. McBride, A.T. Lemley, Environ. Sci. Pollut. Res. 20 (2013) 10-21.
49. S. Song, L. Xu, Z. He, J. Chen, X. Xiao, B. Yan, Environ. Sci. Technol. 41 (2007) 5846-5853.
50. L. Zhou, W. Song, Z. Chen, G. Yin, Environ. Sci. Technol. 47 (2013) 3833-3839.
51. T. Zhu, Y. Li, J. Ji, F.-S. Wong, X. Lu, Sep. Purif. Technol. 62 (2008) 551-558.
52. L. Xu, J.Wang, J. Hazard. Mater. 186 (2011) 256-264.
53. Q.-P. Isariebel, J.-L. Carine, J.-H. Ulises-Javier, W. Anne-Marie, D. Henri, Ultrason. Sonochem. 16 (2009) 610-616.
54. Y. Li, J. Wang, H. Yao, L. Dang, Z. Li, J. Mol. Catal. A: Chem. 334 (2011) 116-122.
55. L. Xu, J. Wang, Environ. Eng. Sci. 30: 6 (2013).

*Graphical Abstract

GRAPHICAL ABSTRACT



HIGHLIGHTS

- Tuning easy parameters of glidarc leads to MnO_2 with different polymorphisms
- Glidarc reduction of $KMnO_4$ leads to α- (high voltage) and δ-MnO_2 (low voltage)
- Glidarc oxidation of Mn acetate leads to γ- (high voltage) and δ-MnO_2 (low voltage)
- Specific areas of MnO_2 increase with increase of glidarc voltage and airflow
- Catalytic bleaching of TY dye greatly depends on the crystalline nature of MnO_2